

# The Hydro-electro-thermal Performance of Air-cooled, Open-cathode Polymer Electrolyte Fuel Cells: Combined Localised Current Density, Temperature and Water Mapping

Meyer, Q, Ashton, S, Jervis, R, Finegan, DP, Boillat, P, Cochet, M, Curnick, O, Reisch, T, Adcock, P, Shearing, PR & Brett, DJL  
Author post-print (accepted) deposited by Coventry University's Repository

## Original citation & hyperlink:

Meyer, Q, Ashton, S, Jervis, R, Finegan, DP, Boillat, P, Cochet, M, Curnick, O, Reisch, T, Adcock, P, Shearing, PR & Brett, DJL 2015, 'The Hydro-electro-thermal Performance of Air-cooled, Open-cathode Polymer Electrolyte Fuel Cells: Combined Localised Current Density, Temperature and Water Mapping' *Electrochimica Acta*, vol. 180, pp. 307-315.

<https://dx.doi.org/10.1016/j.electacta.2015.08.106>

DOI 10.1016/j.electacta.2015.08.106

ISSN 0013-4686

Publisher: Elsevier

**NOTICE: this is the author's version of a work that was accepted for publication in *[Electrochimica Acta]*. Changes resulting from the publishing process, such as peer review, editing, corrections, structural formatting, and other quality control mechanisms may not be reflected in this document. Changes may have been made to this work since it was submitted for publication. A definitive version was subsequently published in *[Electrochimica Acta]*, [180], (2015) DOI: [10.1016/j.electacta.2015.08.106]**

© 2015, Elsevier. Licensed under the Creative Commons Attribution-NonCommercial-NoDerivatives 4.0 International

<http://creativecommons.org/licenses/by-nc-nd/4.0/>

Copyright © and Moral Rights are retained by the author(s) and/ or other copyright owners. A copy can be downloaded for personal non-commercial research or study, without prior permission or charge. This item cannot be reproduced or quoted extensively from without first obtaining permission in writing from the copyright holder(s). The content must not be changed in any way or sold commercially in any format or medium without the formal permission of the copyright holders.

**This document is the author's post-print version, incorporating any revisions agreed during the peer-review process. Some differences between the published version and this version may remain and you are advised to consult the published version if you wish to cite from it.**

1  
2  
3  
4  
5 **The Hydro-electro-thermal Performance of Air-cooled, Open-cathode Polymer**  
6 **Electrolyte Fuel Cells: Combined Localised Current Density, Temperature and**  
7 **Water Mapping**  
8  
9

10  
11  
12 Quentin Meyer<sup>1</sup>, Sean Ashton<sup>2</sup>, Rhodri Jervis<sup>1</sup>, Donal P. Finegan<sup>1</sup>, Pierre Boillat<sup>3,4</sup>,  
13 Magali Cochet<sup>3</sup>, Oliver Curnick<sup>2</sup>, Tobias Reisch<sup>2</sup>, Paul Adcock<sup>2</sup>, Paul R. Shearing<sup>\*1,5</sup>,  
14  
15  
16 Dan J. L. Brett<sup>\*1</sup>  
17  
18  
19

20  
21 <sup>1</sup>Electrochemical Innovation Lab, Department of Chemical Engineering, UCL,  
22 London, WC1E 7JE, United Kingdom.  
23  
24

25  
26 <sup>2</sup>Intelligent Energy, Charnwood Building Holywell Park, Ashby Road, Loughborough  
27 Leicestershire, LE11 3GB, United Kingdom.  
28  
29

30  
31  
32 <sup>3</sup>Electrochemistry Laboratory (LEC), Paul Scherrer Institute (PSI), 5232 Villigen,  
33 Switzerland.  
34  
35  
36

37  
38 <sup>4</sup>Neutron Imaging and Activation Group (NIAG), Paul Scherrer Institute (PSI), 5232  
39 Villigen, Switzerland.  
40  
41  
42

43  
44 <sup>5</sup>UCL/Zeiss Centre for Correlative X-ray Microscopy, UCL, London, WC1E 7JE,  
45 United Kingdom  
46  
47  
48

49  
50 \* Author to whom correspondence should be addressed

51  
52 Tel.: +44(0)20 7679 3310

53  
54 Web: [www.ucl.ac.uk/electrochemical-innovation-lab](http://www.ucl.ac.uk/electrochemical-innovation-lab)

55  
56 Email: [d.brett@ucl.ac.uk](mailto:d.brett@ucl.ac.uk); [p.shearing@ucl.ac.uk](mailto:p.shearing@ucl.ac.uk)  
57  
58  
59

1  
2  
3  
4  
5 **Abstract**  
6  
7

8 *In situ* diagnostic techniques provide a means of understanding the internal workings  
9 of fuel cells so that improved designs and operating regimes can be identified. Here,  
10 a novel metrology approach is reported that combines current and temperature  
11 mapping with water visualisation using neutron radiography.  
12  
13  
14  
15

16 The approach enables a hydro-electro-thermal performance map to be generated  
17 that is applied to an air-cooled, open-cathode polymer electrolyte fuel cell. This type  
18 of fuel cell exhibits a particularly interesting coupled relationship between water,  
19 current and heat, as the air supply has the due role of cooling the stack as well as  
20 providing the cathode reactant feed via a single source. It is found that water  
21 predominantly accumulates under the cooling channels (thickness of 70-100  $\mu\text{m}$   
22 under the cooling channels and 5-25  $\mu\text{m}$  in the active channels at 0.5 A  $\text{cm}^{-2}$ ), in a  
23 similar fashion to the lands in a closed-cathode design, but contrary to passive open-  
24 cathode systems. The relationship between current, temperature and water  
25 accumulation is complex and highly dependent on location within the cell. However,  
26 there is a general trend that higher currents and cooling limitations, especially above  
27 0.7 A  $\text{cm}^{-2}$  and below  $3.9 \times 10^{-3} \text{ m}^3 \text{ s}^{-1}$ , leads to temperatures above 60  $^{\circ}\text{C}$ , which  
28 dehydrate the membrane (water thickness of 10-25  $\mu\text{m}$ ) and the cell operates below  
29 0.5 V.  
30  
31  
32  
33  
34  
35  
36  
37  
38  
39  
40  
41  
42  
43  
44  
45  
46  
47  
48  
49  
50  
51  
52

53 **Keywords**  
54

55 Air-cooled open-cathode polymer electrolyte fuel cell; water mapping; neutron  
56 imaging; temperature mapping; current mapping.  
57  
58  
59  
60  
61  
62  
63  
64  
65

1  
2  
3  
4  
5  
6  
7  
8  
9  
10  
11  
12  
13  
14  
15  
16  
17  
18  
19  
20  
21  
22  
23  
24  
25  
26  
27  
28  
29  
30  
31  
32  
33  
34  
35  
36  
37  
38  
39  
40  
41  
42  
43  
44  
45  
46  
47  
48  
49  
50  
51  
52  
53  
54  
55  
56  
57  
58  
59  
60  
61  
62  
63  
64  
65

## 1. Introduction

Polymer electrolyte fuel cells (PEFC) fuelled with hydrogen are among the most promising energy conversion technologies for a broad range of applications, including portable, stationary and automotive power delivery. A range of diagnosis techniques have been developed to understand and improve the heat and water management in these devices with a view to improving performance, extending durability and informing advanced design.

### 1.1. Current and temperature mapping in fuel cells

Current mapping studies have proven to be insightful and revealed large current density gradients attributed to factors such as: uneven fuel consumptions [1–4], operating conditions [5–7], stoichiometric ratios [8–11], the reactant flow orientation [3,7], and water management issues [12].

Temperature distribution has also been extensively studied, identifying areas of higher electrochemical activity, hot-spot formation and fuel depletion. Thermocouples can provide a crude measure of temperature inside fuel cells [13–16] but cannot provide high spatial resolution. Moreover, thermocouples need to be inserted inside the fuel cell, which often requires design modifications. In contrast, infrared thermal imaging can provide very high spatial and temperature resolution [17–22], yet typically requires use of modified fuel cells with an infrared transparent window, or is otherwise confined to open-cathode fuel cells [23–25] or the outer surface of a cell or stack [26,27].

1  
2  
3  
4  
5 Combined temperature and current mapping studies offer an extra dimension of  
6 information and allow the impact of each parameter on the other to be assessed  
7 [15,26,19,27]; however, the other important component in this equation, water,  
8 needs to be considered in unison to see the whole picture.  
9

## 14 **1.2. Liquid water mapping in fuel cells**

15  
16 Effective water management is of paramount importance for fuel cell operation  
17 (dehydration / flooding can lead to performance decay and stack failure). Water  
18 generation and removal, and transport processes in the gas diffusion layer,  
19 membrane and flow-field have been extensively modelled [30–36]. However, the  
20 reliability of these models depends on the level of validation, which requires  
21 appropriate experimental inputs. Therefore, a number of experimental methods have  
22 been investigated, in order to evaluate, quantify, measure and / or visualise the  
23 water dynamics and distribution under different modes of operation. Such techniques  
24 should ideally satisfy three requirements as defined by Stumper *et al.* [37]: (i) *in situ*  
25 applicability, (ii) minimal invasiveness and (iii) ability to provide information on the  
26 distribution of liquid water over the active area.  
27  
28  
29  
30  
31  
32  
33  
34  
35  
36  
37  
38  
39

40 High frequency impedance enables the ohmic resistance of a fuel cell to be  
41 measured, which can be used to monitor changes in the membrane conductivity, and  
42 therefore hydration content [1,7,16,29,38–44]. Localised electrochemical impedance  
43 spectroscopy (EIS) has been achieved as well, and provides more insight on the  
44 hydration / dehydration processes distributed across electrodes [1,5,29,45].  
45  
46  
47  
48  
49

50  
51  
52 To investigate water content, it is possible to weigh the fuel cell before and after  
53 operation [46], or to visualise liquid water via optical imaging open channels [24,47].  
54 These methods are attractive because of their simplicity, but the most powerful  
55 method for water visualisation, (satisfying all three criteria from Stumper *et al.* [37]) is  
56  
57  
58  
59  
60

1  
2  
3  
4  
5 neutron imaging. This technique is based on attenuation of a neutron by hydrogen-  
6 containing compounds such as water, and transparency to neutrons of most fuel cell  
7 construction materials (aluminium, stainless steel). Neutron imaging can identify  
8 water in the in-plane orientation (with the membrane plane parallel to the beam) and  
9 through-plane orientation (with the membrane plane perpendicular to the beam),  
10 enabling in the first case to differentiate the water content from the cathode and the  
11 anode [48–50] and in the second case the effect of different designs, components,  
12 and operating conditions [45,51–65]. Neutron imaging has been combined with other  
13 modelling and experimental techniques, such as current mapping [66], CFD models  
14 validation [32,51,65], optical imaging [47], neutron scattering [61] and localised EIS  
15 [45].  
16  
17  
18  
19  
20  
21  
22  
23  
24  
25  
26  
27  
28  
29

### 30 **1.3. Air-cooled, Open-Cathode Fuel Cells**

31 Unlike conventional closed-cathode fuel cells, self-breathing fuel cells offer the  
32 advantages of simpler design and integration into systems, using diffusion from the  
33 atmosphere without compressors. Passive air-breathing systems are typically limited  
34 to a maximum current density of  $\sim 0.6 \text{ A cm}^{-2}$  [67–71] due to heat and water  
35 management issues, since water cannot be removed from the membrane, except  
36 through evaporation [69,72]. In the so-called ‘air-cooled, open-cathode’  
37 configuration, air is forced through the cathode channels using fans, which improves  
38 performance and enables higher current densities to be attained [73–77]. In air-  
39 cooled, open-cathode systems the temperature depends on the voltage and current  
40 density [46,67], air cooling flow rate [73,76], and heat transfer characteristics of the  
41 stack. Temperature monitoring is therefore crucial to ensure effective and durable  
42 operation. In practice, this is normally performed using a single-point thermocouple  
43 inserted in the centre of the cell [16,26,75], or for development work using multiple  
44 micro thermocouple measurements at various locations in the fuel cell [13,78,79].  
45  
46  
47  
48  
49  
50  
51  
52  
53  
54  
55  
56  
57  
58  
59  
60  
61  
62  
63  
64  
65

1  
2  
3  
4  
5 Here, we present the results obtained by applying a novel metrology approach to an  
6 air-cooled, open-cathode two-cell stack, operated without external humidification: the  
7 technique combines water visualisation using neutron imaging, with current and  
8 temperature mapping using a printed circuit board (PCB) sensor plate [80]. The  
9 effect and relationship between the key hydro-electro-thermal properties allows  
10 important new insight into this type of fuel cell to be achieved.  
11  
12  
13  
14  
15  
16  
17

## 18 **2. Experimental**

19  
20  
21  
22  
23 *Fuel cell testing* - A 2-cell (60 cm<sup>2</sup> active area) air-cooled / air-breathing fuel cell  
24 stack was used for testing (Intelligent Energy Ltd., UK). The membrane electrode  
25 assembly was composed of commercially available gas diffusion layers (GDLs) and  
26 commercially available membranes with Pt loading of 0.1 and 0.4 mg cm<sup>-2</sup> on the  
27 anode and cathode, respectively.  
28  
29  
30  
31  
32

33  
34 The test station [26] supplied dry hydrogen at ambient temperature (with a purity of  
35 99.995 %) to the anodes and air was forced through the stack by a single fan  
36 (SanAce 36, Sanyo Denki) to the open-cathode channels (Figure 1). The exhaust  
37 hydrogen flow rate in through-flow mode was measured using a thermal mass flow  
38 meter (MassVIEW, Bronkhorst) to be 4.7 SLPM, which ensures a stoichiometric ratio  
39 of 2 at 1 A cm<sup>-2</sup>. The fans, which provide cooling and air supply to the cathode, were  
40 controlled by a programmable power supply (3649A Agilent). The current drawn from  
41 the PEFC was controlled using an electronic load (PLZ664WA, Kikusui) in  
42 galvanostatic mode. An in-house computer controlled system controls the air,  
43 hydrogen, cooling and electrical valves (LabVIEW, National Instruments) as well as  
44 recording and presenting data using a data acquisition card (USB 6363, National  
45 Instruments). Ambient temperature, pressure (absolute) and relative humidity (RH)  
46 were measured at 25 °C ± 0.2 °C, 0.97 ± 0.02 bar and 40% RH respectively, during  
47  
48  
49  
50  
51  
52  
53  
54  
55  
56  
57  
58  
59  
60

1  
2  
3  
4  
5 all tests. The operation of this fuel cell in terms of cathode design, cooling and active  
6 channels and materials [26,27], temperature uncertainty [27] and water management  
7 in dead-ended anode mode [26], has been described in previous reports. In this work  
8 the anode and cathode are operated in through-flow mode.  
9  
10  
11  
12  
13

#### 14 *Current and temperature mapping*

15  
16 Current and temperature mapping were performed using a 16-segment printed  
17 circuit board sensor plate (S++ Simulation Services, Germany). Each segment  
18 covers an area of 3.75 cm<sup>2</sup>. The temperature is measured using copper ‘meanders’  
19 with a 2 mA current applied, as the resistance of copper is very sensitive to  
20 temperature changes; the local current at each contact was measured using shunt  
21 resistors made of a special alloy insensitive to temperature changes. Further details  
22 on the approach can be found in previously published work.[80]  
23  
24  
25  
26  
27  
28  
29  
30  
31

#### 32 *Neutron imaging facility*

33  
34 Neutron radiography was performed at the neutron imaging facility NEUTRA of the  
35 SINQ spallation source (Paul Scherrer Institute, Switzerland) [81]. Thermal neutrons  
36 provided by the source are extracted from a moderator tank in the thermal energy  
37 range of  $1 \times 10^{-3}$  to 10 eV with a Maxwellian spectrum energy of  $25 \times 10^{-3}$  eV. The  
38 third position was used on the beamline since it offers a beam diameter of 40 cm  
39 [81], and a maximal detector field of view of 36 × 38 cm, hence suitable for larger  
40 scale samples. In order to image the water distribution over the entire surface of the  
41 electrodes area, the cell faced the neutron beam in through-plane orientation (Figure  
42 1 a-b). The detector consists of a neutron-sensitive LiF/ZnS scintillator and a charge-  
43 coupled CCD device (Ikon-L, Andor) camera housed in a light-tight box (Figure 1 a).  
44 The neutron beam is converted into a photonic field by the scintillator, whereby the  
45 intensity of evoked light is proportional to the intensity of the incoming neutron beam  
46 [56].  
47  
48  
49  
50  
51  
52  
53  
54  
55  
56  
57  
58  
59  
60  
61  
62  
63  
64  
65

1  
2  
3  
4  
5  
6  
7 Measurements were performed with an exposure time of 10 s (time during which the  
8 camera opens a built-in shutter and integrates the light), and a sampling time of 2-3 s  
9 per image (time during which the image is processed), for sufficient resolution and  
10 noise reduction. This exposure time is well within the range typically used for neutron  
11 imaging on PEFCs (typically between 1 and 25 s [45,51–59,82]). Since the current  
12 study investigates steady-state operation, the 12 s temporal resolution is sufficient.  
13  
14 The intensity images are generated in FITS format, and are processed using PSI in-  
15 house software written in the IDL language.  
16  
17  
18  
19  
20  
21  
22  
23  
24

#### 25 *Quantification of the water thickness from neutron images*

26 All the materials of the cell contribute to the attenuation of the transmitted neutron  
27 beam, following the Beer-Lambert law (Equation 1).  
28  
29  
30  
31

$$32 \quad I/I_0 = \exp(-\mu_{water}t_{water}) \quad (1)$$

33  
34 With  $I$  the intensity of the beam in operation,  $I_0$  the intensity of the beam for the dry  
35 cell (without water),  $\mu_{water}$  the attenuation coefficient of water,  $t_{water}$  the thickness of  
36 water.  $I$  and  $I_0$  are determined after all necessary corrections (filtering, subtraction of  
37 background components, alignment of “working” and reference images) [83].  
38  
39  
40  
41  
42  
43

44 The water thickness is then extracted by taking the logarithm, divided by the  
45 attenuation coefficient  $\mu_{water}$ .  
46  
47  
48  
49

$$50 \quad t_{water} = -\frac{\ln(I/I_0)}{\mu_{water}} \quad (2)$$

51  
52  
53  
54 In our case,  $\mu_{water}$ , the attenuation coefficient of neutrons in liquid water, was  
55 measured in the NEUTRA beamline for the given setup at  $3.5 \text{ cm}^{-1}$  [84]. In the  
56  
57  
58  
59  
60  
61  
62  
63  
64  
65

1  
2  
3  
4  
5 following sections, the water content will be expressed as the effective water  
6 thickness  $t_{water}$  in  $\mu\text{m}$ .  
7  
8  
9

### 10 **3. Results**

#### 11 **3.1. Sensor plate neutron transparency**

12  
13  
14  
15  
16  
17  
18 The sensor plate was imaged at the Paul Scherrer Institute prior to its insertion in the  
19 stack and was found to be 80 % transparent, which is suitable for imaging.  
20 Therefore, the combined neutron imaging and current and temperature mapping is  
21 possible with this choice of hardware. The sensor plate is inserted between the first  
22 and the second cell (Figure 2c), to measure the average current and temperature  
23 distribution of both cells.  
24  
25  
26  
27  
28  
29  
30  
31  
32  
33

#### 34 **3.2. Neutron imaging for water visualisation**

35  
36  
37  
38 Although high frequency EIS provides a useful indication of the membrane  
39 conductivity, it is limited in spatial resolution to the size of the localised current  
40 collector. In EIS, it is common to assume that changes in the purely Ohmic  
41 resistance are due to the electrolyte membrane (and its water content); however,  
42 other factors such as changes in contact resistance associated with membrane  
43 swelling can complicate interpretation of this electrical measurement. Neutron  
44 imaging allows a high resolution map of the water distribution to be generated that  
45 can unequivocally discern between the water in the channel and under the land  
46 positions. It is the combination of these techniques, with knowledge of the local  
47 temperature, that makes this correlative approach particularly powerful.  
48  
49  
50  
51  
52  
53  
54  
55  
56  
57  
58  
59  
60  
61  
62  
63  
64  
65

1  
2  
3  
4  
5 The stack technology investigated uses an electrically insulating layer between the  
6 endplates and the current collector / bipolar plates. This is relatively opaque to  
7 neutrons; therefore, a modification was made to the insulating layer so as to retain  
8 functionality but allow substantial open areas so that water imaging could take place.  
9 This resulted in the opaque pattern shown in Figure 2 (a-b). Since the cell is  
10 operated using dry gases, at open circuit potential, it does not have any water  
11 (Figure 2a).  
12  
13  
14  
15  
16  
17  
18  
19  
20

21 Throughout this study, a two cell stack is imaged, for enhancement of water  
22 detection and behaviour closer to stack operation (Figure 2 c). A water 'thickness' of  
23 75  $\mu\text{m}$  per cell is within the range of water contents previously reported for single  
24 cells (30 - 2000  $\mu\text{m}$ ) [47,54,55,85,86].  
25  
26  
27  
28  
29

30 Under practical operation of this commercial stack technology, a single thermocouple  
31 is inserted into the central cooling channel for monitoring and control purposes.  
32 Therefore, when considering overall performance compared to cell temperature and  
33 average current density, the water content of the central cooling channel (Figure 2 b)  
34 is used.  
35  
36  
37  
38  
39  
40

41 A special variation in water thickness is consistently observed, as seen by the  
42 repeating sequence of blue and yellow regions in Figure 2 b. From the enhanced  
43 view, correlated with the cathode plate geometry (Figure 2 c-d), it is clear that the  
44 area under the cooling channels contains most of the water. This is an important  
45 finding and contrasts with self-breathing fuel cells where substantial build-up of water  
46 in open channels has been identified using neutron imaging and standard  
47 visualisation techniques [24,49]. Here, the very high flow rate of air through the  
48 active channels ( $5.6 \times 10^{-3} \text{ m}^3 \text{ s}^{-1}$ ) dehydrates the fuel cell in locations directly under  
49 the open channels by constantly removing most of the water vapour and liquid water  
50  
51  
52  
53  
54  
55  
56  
57  
58  
59  
60

1  
2  
3  
4  
5 droplets, substantially hindering its accumulation. On the other hand, in the cooling  
6 channels, the cold air cools down the metal plate without removing any of the water,  
7 since the electrode is not in direct contact with the air stream.  
8  
9

10 This result agrees with the model of Xing et al. [36], which describes 10 times more  
11 water under the rib than under the channel areas. This feature is also in agreement  
12 with the measurements performed under the ribs and channels in closed-cathode  
13 configuration, with a dry cathode. The water almost exclusively concentrated under  
14 the land, and not under the channels [82,87].  
15  
16  
17  
18  
19  
20  
21

22 Since the cell is imaged in through-plane mode, it is not possible to assess the  
23 location of the water through the thickness of the cell, and differentiate between  
24 water in the channel, GDL or membrane. Rather, the through-plane technique  
25 provides a quantitative measure of total water content through the plane of the fuel  
26 cell at that point.  
27  
28  
29  
30  
31  
32  
33  
34  
35  
36

### 37 **3.3. Hydro-Electro-thermal performance analysis**

38  
39  
40 To understand how the fuel cell's performance is affected by the distribution of water,  
41 it is necessary to characterise how the water content is affected by the air flow rate  
42 and current density. This is first investigated on a whole-cell scale, looking at the  
43 effect of the current and air flow rate on the voltage, temperature and average water  
44 content in a cooling channel in the centre of the cell. For further analysis, the  
45 localised distributions are investigated via current, temperature and water mapping  
46 as a single dataset in the hydro-electro-thermal analysis.  
47  
48  
49  
50  
51  
52  
53  
54  
55  
56  
57  
58  
59  
60  
61  
62  
63  
64  
65

1  
2  
3  
4  
5 **3.3.1. Hydro-electro-thermal profile as a function of the air flow rate and**  
6 **current density.**  
7  
8  
9

10 Electro-thermal performance maps have been introduced in previous work as a  
11 novel way to display the influence of the air flow rate and current density on the  
12 voltage and temperature of fuel cell operation [88]. Including the water content  
13 provides another dimension in understanding the coupled nature of processes  
14 occurring in operational fuel cells.  
15  
16  
17  
18  
19

20  
21  
22 To acquire the 'map' data, a series of four air flow rates, 2.7, 3.9, 4.7 and  $5.6 \times 10^{-3}$   
23  $\text{m}^3 \text{s}^{-1}$  were investigated, holding the voltage constant for 10 minutes to obtain steady  
24 state performance, from open circuit, with an increment of  $0.083 \text{ A cm}^{-2}$ , and the  
25 polarisation was interrupted once the voltage dropped below 0.5 V. The entire test,  
26 adding an extra 15 minutes to leave the cell to dry and reach ambient temperature  
27 between changes of flow rate, lasted 8 hours. Overall, 42 different conditions of  
28 current densities and air flow rates were measured. The hydro-thermal profile  
29 represents the influence of the air flow rate and current density on the mean cell  
30 voltage, and water thickness and temperature of the central cooling channel. It was  
31 generated by averaging the neutron images for the last 10 frames (2 minutes) prior  
32 to the change of current density, then extracting with ImageJ<sup>®</sup> the average water  
33 thickness in the central cooling channel (Figure 2).  
34  
35  
36  
37  
38  
39  
40  
41  
42  
43  
44  
45  
46  
47

48 The 'electro-thermal' map is coupled with the 'hydro-thermal' map, to form a so-  
49 called 'hydro-electro-thermal' profile; this allows analysis of the link between current  
50 density, temperature, water content and air flow rate (Figure 3).  
51  
52  
53  
54  
55

56 An initial hydration of the cell occurs between 0 and  $0.4 \text{ A cm}^{-2}$ , in the activation and  
57 beginning of the ohmic predominance region. This is the cell self-hydration, as the  
58  
59  
60  
61  
62  
63  
64  
65

1  
2  
3  
4  
5 amount of water generated increases with increasing load, as described by  
6 Faraday's Law; while the low temperature (<40 °C) is in favour of water  
7 condensation [89]. A maximum hydration is reached between 35 and 45 °C, for a  
8 current density between 0.35 and 0.67 A cm<sup>-2</sup> for low and high air flow rate,  
9 respectively. This corresponds to the centre of the ohmic region on the electro-  
10 thermal map. It overlaps with the optimum operating zone, determined using the  
11 current of lowest resistance, introduced in previous work [88]. Gradual dehydration  
12 starts above 45 °C, with a 'dry' state reached above 60°C.  
13  
14  
15  
16  
17  
18  
19  
20  
21

22  
23 These results confirm the conclusions from previous work based on electro-thermal  
24 profiles alone [88], which showed that the purely ohmic resistance (proxy for  
25 membrane hydration) initially drops (during self-hydration), reaches a plateau, and  
26 then increases above 60°C during the dehydration. This hydration / dehydration  
27 process has been experimentally reported for self-breathing, open-cathode fuel cells  
28 [46], and modelled [89]; but only now can the role of water be confirmed.  
29  
30  
31  
32  
33  
34  
35

36  
37 To fully understand the hydro-electro-thermal process and its direct influence on the  
38 voltage decay across a polarisation, it is necessary to investigate the localised maps  
39 and full scale neutron images.  
40  
41  
42  
43  
44  
45

### 46 **3.3.2. Locally resolved hydro-electro-thermal maps.**

47  
48  
49

50  
51 In order to understand how the current density, temperature and the water content  
52 locally affect performance, spatial maps for each quantity were investigated in unison  
53 for a given current density and air flow rate. The water maps were generated using  
54 the averaging over 2 minutes prior to the change of current density.  
55  
56  
57  
58  
59  
60  
61  
62  
63  
64  
65

1  
2  
3  
4  
5 At open circuit potential, the cell is entirely dry, as discussed earlier (Figure 2a) and  
6 has an even temperature of  $25 \pm 0.2^\circ\text{C}$  across the cell (ambient).  
7  
8  
9

10  
11 The operating points labelled (a) to (f) in Figure 3 were selected to represent the  
12 range of operation from 'low' (a-b, between  $25\text{-}40^\circ\text{C}$ ), 'intermediate' (c-d, between  
13  $40\text{-}50^\circ\text{C}$ ) and 'high' current densities (e-f between  $50\text{-}75^\circ\text{C}$ ). Initially, at (a), (Figure  
14 4), water is only observed towards the air exhaust, and in the cooling channels ( $10\text{-}$   
15  $15\ \mu\text{m}$ ). This water gradient is caused by the higher current density ( $0.097\text{-}0.085\ \text{A}$   
16  $\text{cm}^{-2}$ ), whereas it is lower near the air inlet ( $0.078\text{-}0.071\ \text{A}\ \text{cm}^{-2}$ ). The temperature  
17 variation across the cell is only  $1^\circ\text{C}$ . For all of the points measured (a-f) there is a  
18 general decrease in current density from the hydrogen inlet to outlet (left to right in  
19 the figures), this is associated with consumption of the hydrogen as it flow through  
20 the cell.  
21  
22  
23  
24  
25  
26  
27  
28  
29

30 At (b), the hydro map reveals that the cell has fully self-hydrated, with water present  
31 in the entire cooling channel ( $40\text{-}100\ \mu\text{m}$ ), and to some extent in the active channels  
32 ( $5\ \mu\text{m}$ ). Higher water content is observed near the air exhaust with  $75\text{-}90\ \mu\text{m}$ , against  
33  $40\text{-}45\ \mu\text{m}$  near the air inlet, consistent with the current density gradient. The higher  
34 temperature near the air exhaust increases the reaction rate, hence causing a higher  
35 current density.  
36  
37  
38  
39  
40  
41  
42  
43

44 Relatively uniform water profiles exist under the cooling channels across the extent  
45 of the cell at (c) and (d) (Figure 5). Although the current density is higher near the air  
46 exhaust, and will result in more water generation, more water evaporates due to the  
47 higher temperature ( $\sim 40^\circ\text{C}$ ); hence water distribution is balanced along the air  
48 channel direction.  
49  
50  
51  
52  
53

54  
55  
56 Closer analysis of the water content along the central channel for point (c) and (d) is  
57 shown in Figure 6. The quantitative profiles show that despite generating more  
58  
59  
60

1  
2  
3  
4  
5 current in (d), the higher temperature leads to greater evaporation and a decrease in  
6 the water thickness. Effectively, the entire cell is starting to dehydrate, with an  
7 increase in the evaporation rate.  
8  
9

10  
11  
12  
13  
14  
15 Figure 7 shows two points (e-f), into the dehydration zone, with distinctively different  
16 features from the ones observed in a-d. As the total current increases, the regime  
17 of operation changes such that a combination of factors result in a local minimum in  
18 the current distribution along the air channel flow direction, as seen in (e). The  
19 substantial increase in temperature towards the air exhaust acts to evaporate water  
20 from the MEA, compromising membrane hydration and limiting the ability to generate  
21 more current. However, the cooling effect of the air intake means that the entrance  
22 region retains hydration, allowing the current to continue to increase.  
23  
24  
25  
26  
27  
28  
29  
30

31  
32  
33 As the load is increased further into region (f), the cell temperature towards the air  
34 exit reaches 74 °C and the cell is substantially dehydrated. The water profile is now  
35 inverted from that at point (a), a slight amount of water only discernible near the air  
36 inlet (5-15 µm). This means that the current is now greatest at the air inlet and goes  
37 through a minimum further along the air channel.  
38  
39  
40  
41  
42  
43

44  
45 Overall, this cell dehydration is caused by the limitations in the cooling. The hydro-  
46 electro-thermal mapping reveals that evenly distributed amounts of water across the  
47 cell ensure stable and optimum performance. Operations around 45 to 50 °C at high  
48 load hinders water evaporation. Therefore, this is a target for the operations of air-  
49 cooled open cathode fuel cells. Up to a point, increasing the air flow rate would  
50 regulate the temperature and enable higher loads; however, the subsequent  
51 parasitic power losses would significantly increase, as highlighted in previous studies  
52 [90], and a suitable trade-off needs to be determined.  
53  
54  
55  
56  
57  
58  
59

1  
2  
3  
4  
5  
6  
7  
8 **4. Conclusion**  
9

10  
11  
12 A new approach for probing the operation of open-cathode, air-breathing fuel cells  
13 has been presented that uses a 'hydro-electro-thermal' mapping process through the  
14 combined use of water imaging, current and temperature mapping. This  
15 methodology allows the action of hydration and dehydration to be studied under  
16 different load and flow rate conditions and allows zones of optimal operation to be  
17 identified. Water accumulates mainly under the cooling channels, which is  
18 analogous to the land in conventional closed-cathode systems.  
19  
20  
21  
22  
23  
24  
25  
26

27  
28 Water removal within the cell is determined by local temperature, flow of air in the  
29 active channels and the transport of water from under the cooling channels into the  
30 active channels. Other factors are likely to affect the transport of water, such as the  
31 gas diffusion layer thickness, porosity, hydrophobicity and degree of compression, as  
32 well as the electrolyte membrane properties.  
33  
34  
35  
36  
37  
38

39  
40 Finally, it should be noted that all three techniques are required to be used in unison  
41 in order to obtain a complete picture of water management. This approach allows the  
42 complex mechanisms that determine the generation, accumulation, transport and  
43 removal of water in operating fuel cells to be investigated.  
44  
45  
46  
47  
48  
49

50  
51 **5. Acknowledgements**  
52

53  
54 The authors would like to acknowledge the EPSRC for supporting the  
55 Electrochemical Innovation Lab through (EP/M009394/1, EP/G030995/1,  
56 EP/I037024/1, EP/M014371/1 and EP/M023508/1). The authors acknowledge the  
57  
58  
59  
60

1  
2  
3  
4  
5 support of Intelligent Energy and UCL for supporting the studentship of Meyer,  
6  
7 EPSRC ELEVATE project for currently supporting Meyer and the RAEng for  
8  
9 supporting Shearing. The neutron imaging work was carried out with the support of  
10  
11 the European Community. The authors appreciate the support of the European  
12  
13 Research Infrastructure H2FC (funded under the FP7 specific programme  
14  
15 Capacities, Grant Agreement Number 284522) and its partner PSI. Financial support  
16  
17 by the Austrian Ministry of Transport, Innovation and Technology (BMVIT) and The  
18  
19 Austrian Research Promotion Agency (FFG) is gratefully acknowledged for the  
20  
21 funding of the A3FALCON Project. We also thank Dr Denis Kramer for many useful  
22  
23 discussions.  
24  
25  
26  
27  
28  
29

## 30 **6. References**

- 31
- 32 [1] D. Gerteisen, W. Mérida, T. Kurz, P. Lupotto, M. Schwager, C. Hebling,  
33 Spatially Resolved Voltage, Current and Electrochemical Impedance  
34 Spectroscopy Measurements, *Fuel Cells*. 11 (2011) 339–349.
- 35 [2] D.J.L. Brett, S. Atkins, N.P. Brandon, V. Vesovic, N. Vasileiadis, A.R. Kucernak,  
36 Measurement of the current distribution along a single flow channel of a solid  
37 polymer fuel cell, *Electrochem. Commun.* 3 (2001) 628–632.
- 38 [3] I. Alaefour, G. Karimi, K. Jiao, S. Al Shakhshir, X. Li, Experimental study on the  
39 effect of reactant flow arrangements on the current distribution in proton  
40 exchange membrane fuel cells, *Electrochim. Acta*. 56 (2011) 2591–2598.
- 41 [4] J. Kleemann, F. Finsterwalder, W. Tillmetz, Characterisation of mechanical  
42 behaviour and coupled electrical properties of polymer electrolyte membrane  
43 fuel cell gas diffusion layers, *J. Power Sources*. 190 (2009) 92–102.
- 44 [5] D.J.L. Brett, S. Atkins, N.P. Brandon, N. Vasileiadis, V. Vesovic, A.R. Kucernak,  
45 Membrane resistance and current distribution measurements under various  
46 operating conditions in a polymer electrolyte fuel cell, *J. Power Sources*. 172  
47 (2007) 2–13.
- 48 [6] M. Santis, S.A. Freunberger, M. Papra, A. Wokaun, N.B. Felix, Experimental  
49 investigation of coupling phenomena in polymer electrolyte fuel cell stacks, *J.*  
50 *Power Sources*. 161 (2006) 1076–1083.
- 51 [7] D. Gerteisen, N. Zamel, C. Sadeler, F. Geiger, V. Ludwig, C. Hebling, Effect of  
52 operating conditions on current density distribution and high frequency  
53 resistance in a segmented PEM fuel cell, *Int. J. Hydrogen Energy*. 37 (2012)  
54 7736–7744.  
55  
56  
57  
58  
59  
60  
61  
62  
63  
64  
65

- 1  
2  
3  
4 [8] M.M. Mench, C.Y. Wang, M. Ishikawa, In Situ Current Distribution  
5 Measurements in Polymer Electrolyte Fuel Cells, *J. Electrochem. Soc.* 150  
6 (2003) A1052–A1059.  
7 [9] J.J. Hwnag, W.R. Chang, R.G. Peng, P.Y. Chen, A. Su, Experimental and  
8 numerical studies of local current mapping on a PEM fuel cell, *Int. J. Hydrogen*  
9 *Energy.* 33 (2008) 5718–5727.  
10 [10] Y. Yu, X.-Z. Yuan, H. Li, E. Gu, H. Wang, G. Wang, et al., Current mapping of a  
11 proton exchange membrane fuel cell with a segmented current collector during  
12 the gas starvation and shutdown processes, *Int. J. Hydrogen Energy.* 37  
13 (2012) 15288–15300.  
14 [11] I. Alaefour, G. Karimi, K. Jiao, X. Li, Measurement of current distribution in a  
15 proton exchange membrane fuel cell with various flow arrangements – A  
16 parametric study, *Appl. Energy.* 93 (2012) 80–89.  
17 [12] F.N. Büchi, A.B. Geiger, R.P. Neto, Dependence of current distribution on water  
18 management in PEFC of technical size, *J. Power Sources.* 145 (2005) 62–67.  
19 [13] M. Wilkinson, M. Blanco, E. Gu, J.J. Martin, D.P. Wilkinson, J.J. Zhang, et al.,  
20 In Situ Experimental Technique for Measurement of Temperature and Current  
21 Distribution in Proton Exchange Membrane Fuel Cells, *Fuel Cell.* 9 (2006)  
22 507–511.  
23 [14] M. Matian, A. Marquis, D. Brett, N. Brandon, An experimentally validated heat  
24 transfer model for thermal management design in polymer electrolyte  
25 membrane fuel cells, *Proc. Inst. Mech. Eng. Part A J. Power Energy.* 224  
26 (2010) 1069–1081.  
27 [15] G. Zhang, L. Guo, L. Ma, H. Liu, Simultaneous measurement of current and  
28 temperature distributions in a proton exchange membrane fuel cell, *J. Power*  
29 *Sources.* 195 (2010) 3597–3604.  
30 [16] O. Lottin, T. Colinart, S. Chupin, S. Didierjean, A multi-instrumented polymer  
31 exchange membrane fuel cell: Observation of the in-plane non-  
32 homogeneities, *J. Power Sources.* 180 (2008) 748–754.  
33 [17] M. Wang, H. Guo, C. Ma, Temperature distribution on the MEA surface of a  
34 PEMFC with serpentine channel flow bed, *J. Power Sources.* 157 (2006) 181–  
35 187.  
36 [18] A. Hakenjos, H. Muentner, U. Wittstadt, C. Hebling, A PEM fuel cell for combined  
37 measurement of current and temperature distribution , and flow field flooding,  
38 *J. Power Sources.* 131 (2004) 213–216.  
39 [19] L.S. Martins, J.E.F.C. Gardolinski, J.V.C. Vargas, J.C. Ordonez, S.C. Amico,  
40 M.M.C. Forte, The experimental validation of a simplified PEMFC simulation  
41 model for design and optimization purposes, *Appl. Therm. Eng.* 29 (2009)  
42 3036–3048.  
43 [20] R. Shimoi, M. Masuda, K. Fushinobu, Y. Kozawa, K. Okazaki, Visualization of  
44 the Membrane Temperature Field of a Polymer Electrolyte Fuel Cell, *J. Energy*  
45 *Resour. Technol.* 126 (2004) 258–261.  
46 [21] M. Matian, A.J. Marquis, N.P. Brandon, Application of thermal imaging to  
47 validate a heat transfer model for polymer electrolyte fuel cells, *Int. J.*  
48 *Hydrogen Energy.* 35 (2010) 12308–12316.  
49 [22] D.J.L. Brett, P. Aguiar, R. Clague, a. J. Marquis, S. Schöttl, R. Simpson, et al.,  
50 Application of infrared thermal imaging to the study of pellet solid oxide fuel  
51 cells, *J. Power Sources.* 166 (2007) 112–119.  
52  
53  
54  
55  
56  
57  
58  
59  
60  
61  
62  
63  
64  
65

- 1  
2  
3  
4 [23] O.A. Obeisun, Q. Meyer, J. Robinson, C.W. Gibbs, A.R. Kucernak, P. Shearing,  
5 et al., Advanced diagnostics applied to a self-breathing fuel cell O. A. Obeisun,  
6 ECS Trans. 61 (2014) 249–258.
- 7 [24] O. Obeisun, Q. Meyer, J. Robinson, C.W. Gibbs, A.R. Kucernak, P.R.  
8 Shearing, et al., Development of open-cathode polymer electrolyte fuel cells  
9 using printed circuit board flow-field plates: Flow geometry characterisation,  
10 Int. J. Hydrogen Energy. 39 (2014) 18326–18336.
- 11 [25] O.A. Obeisun, Q. Meyer, E. Engebretsen, D.P. Finegan, J.B. Robinson, P.R.  
12 Shearing, et al., Effect of current density and flow plate orientation on water  
13 management in an open-cathode fuel cell using thermal imaging, gravimetric  
14 analysis and water droplet visualisation, Int. J. Hydrog. Energy, Submitt. (n.d.).
- 15 [26] Q. Meyer, S. Ashton, O. Curnick, T. Reisch, P. Adcock, K. Ronaszegi, et al.,  
16 Dead-Ended Anode Polymer Electrolyte Fuel Cell Stack Operation  
17 Investigated using Electrochemical Impedance Spectroscopy, Off-gas Analysis  
18 and Thermal Imaging, J. Power Sources. 254 (2013) 1–9.
- 19 [27] M. Noorkami, J.B. Robinson, Q. Meyer, O.A. Obeisun, E.S. Fraga, T. Reisch, et  
20 al., Effect of temperature uncertainty on polymer electrolyte fuel cell  
21 performance5, Int. J. Hydrogen Energy. 39 (2014) 1439–1448.
- 22 [28] K. Jiao, I.E. Alaefour, G. Karimi, X. Li, Simultaneous measurement of current  
23 and temperature distributions in a proton exchange membrane fuel cell during  
24 cold start processes, Electrochim. Acta. 56 (2011) 2967–2982.
- 25 [29] A. Hakenjos, C. Hebling, Spatially resolved measurement of PEM fuel cells, J.  
26 Power Sources. 145 (2005) 307–311.
- 27 [30] T.E. Springer, T.A. Zawodzinski, S. Gottesfeld, Polymer Electrolyte Fuel Cell  
28 Model, J. Electrochem. Soc. 138 (1993) 2334–2342.
- 29 [31] B. Siversten, N. Djilali, CFD-based modelling of proton exchange membrane  
30 fuel cells, J. Power Sources. 141 (2005) 65–78.
- 31 [32] A. Iranzo, P. Boillat, F. Rosa, Validation of a three dimensional PEM fuel cell  
32 CFD model using local liquid water distributions measured with neutron  
33 imaging, Int. J. Hydrogen Energy. 39 (2014) 7089–7099.
- 34 [33] N. Djilali, Computational modelling of polymer electrolyte membrane (PEM) fuel  
35 cells: Challenges and opportunities, Energy. 32 (2007) 269–280.
- 36 [34] Y. Zong, B. Zhou, A. Sobiesiak, Water and thermal management in a single  
37 PEM fuel cell with non-uniform stack temperature, J. Power Sources. 161  
38 (2006) 143–159.
- 39 [35] S. Chaudhary, V.K. Sachan, P.K. Bhattacharya, Two dimensional modelling of  
40 water uptake in proton exchange membrane fuel cell, Int. J. Hydrogen Energy.  
41 39 (2014) 17802–17818.
- 42 [36] L. Xing, X. Liu, T. Alaje, R. Kumar, M. Mamlouk, K. Scott, A two-phase flow and  
43 non-isothermal agglomerate model for a proton exchange membrane (PEM)  
44 fuel cell, Energy. 73 (2014) 618–634.
- 45 [37] J. Stumper, M. Löhr, S. Hamada, Diagnostic tools for liquid water in PEM fuel  
46 cells, J. Power Sources. 143 (2005) 150–157.
- 47 [38] T. Matsuura, J. Chen, J.B. Siegel, A.G. Stefanopoulou, Degradation  
48 phenomena in PEM fuel cell with dead-ended anode, Int. J. Hydrogen Energy.  
49 38 (2013) 11346–11356.
- 50 [39] J. Pino, F. Rosa, A. Iranzo, M. Mun, E. Lo, Experimental fuel cell performance  
51 analysis under different operating conditions and bipolar plate designs, Int. J.  
52 Hydrogen Energy. 5 (2010) 11437–11447.
- 53  
54  
55  
56  
57  
58  
59  
60  
61  
62  
63  
64  
65

- 1  
2  
3  
4 [40] T. Kurz, A. Hakenjos, J. Krämer, M. Zedda, C. Agert, An impedance-based  
5 predictive control strategy for the state-of-health of PEM fuel cell stacks, *J.*  
6 *Power Sources.* 180 (2008) 742–747.  
7  
8 [41] Q. Yan, H. Toghiani, J. Wu, Investigation of water transport through membrane  
9 in a PEM fuel cell by water balance experiments, *J. Power Sources.* 158  
10 (2006) 316–325.  
11 [42] X. Yuan, J.C. Sun, H. Wang, J. Zhang, AC impedance diagnosis of a 500W  
12 PEM fuel cell stack, *J. Power Sources.* 161 (2006) 929–937.  
13 [43] T.J. Mason, J. Millichamp, T.P. Neville, P.R. Shearing, S. Simons, D.J.L. Brett,  
14 A study of the effect of water management and electrode flooding on the  
15 dimensional change of polymer electrolyte fuel cells, *J. Power Sources.* 242  
16 (2013) 70–77.  
17 [44] A. Hakenjos, M. Zobel, J. Clausnitzer, C. Hebling, Simultaneous  
18 electrochemical impedance spectroscopy of single cells in a PEM fuel cell  
19 stack, *J. Power Sources.* 154 (2006) 360–363.  
20 [45] I.A. Schneider, D. Kramer, A. Wokaun, G.G. Scherer, Spatially resolved  
21 characterization of PEFCs using simultaneously neutron radiography and  
22 locally resolved impedance spectroscopy, *Electrochem. Commun.* 7 (2005)  
23 1393–1397.  
24 [46] T. Fabian, J.D. Posner, R. O'Hayre, S.-W. Cha, J.K. Eaton, F.B. Prinz, et al.,  
25 The role of ambient conditions on the performance of a planar, air-breathing  
26 hydrogen PEM fuel cell, *J. Power Sources.* 161 (2006) 168–182.  
27 [47] D. Spornjak, S.G. Advani, A.K. Prasad, Simultaneous Neutron and Optical  
28 Imaging in PEM Fuel Cells, *J. Electrochem. Soc.* 156 (2009) B109.  
29 [48] Y.-S. Chen, H. Peng, D.S. Hussey, D.L. Jacobson, D.T. Tran, T. Abdel-Baset,  
30 et al., Water distribution measurement for a PEMFC through neutron  
31 radiography, *J. Power Sources.* 170 (2007) 376–386.  
32 [49] M. Weiland, P. Boillat, P. Oberholzer, a. Kaestner, E.H. Lehmann, T.J. Schmidt,  
33 et al., High resolution neutron imaging for pulsed and constant load operation  
34 of passive self-breathing polymer electrolyte fuel cells, *Electrochim. Acta.* 87  
35 (2013) 567–574.  
36 [50] P. Boillat, D. Kramer, B.C. Seyfang, G. Frei, E. Lehmann, G.G. Scherer, et al.,  
37 In situ observation of the water distribution across a PEFC using high  
38 resolution neutron radiography, *Electrochem. Commun.* 10 (2008) 546–550.  
39 [51] A. Iranzo, P. Boillat, P. Oberholzer, J. Guerra, A novel approach coupling  
40 neutron imaging and numerical modelling for the analysis of the impact of  
41 water on fuel cell performance, *Energy.* 68 (2014) 971–981.  
42 [52] J. Zhang, D. Kramer, R. Shimoi, Y. Ono, E. Lehmann, A. Wokaun, et al., In situ  
43 diagnostic of two-phase flow phenomena in polymer electrolyte fuel cells by  
44 neutron imaging, *Electrochim. Acta.* 51 (2006) 2715–2727.  
45 [53] P. Oberholzer, P. Boillat, R. Siegrist, R. Perego, a. Kästner, E. Lehmann, et al.,  
46 Cold-Start of a PEFC Visualized with High Resolution Dynamic In-Plane  
47 Neutron Imaging, *J. Electrochem. Soc.* 159 (2012) B235.  
48 [54] E.H. Lehmann, P. Boillat, G. Scherrer, G. Frei, Fuel cell studies with neutrons  
49 at the PSI's neutron imaging facilities, *Nucl. Instruments Methods Phys. Res.*  
50 *Sect. A Accel. Spectrometers, Detect. Assoc. Equip.* 605 (2009) 123–126.  
51 [55] J.B. Siegel, D.A. McKay, A.G. Stefanopoulou, D.S. Hussey, D.L. Jacobson,  
52 Measurement of Liquid Water Accumulation in a PEMFC with Dead-Ended  
53 Anode, *J. Electrochem. Soc.* 155 (2008) B1168–B1178.  
54  
55  
56  
57  
58  
59  
60  
61  
62  
63  
64  
65

- 1  
2  
3  
4 [56] D. Kramer, J. Zhang, R. Shimoi, E. Lehmann, A. Wokaun, K. Shinohara, et al.,  
5 In situ diagnostic of two-phase flow phenomena in polymer electrolyte fuel  
6 cells by neutron imaging, *Electrochim. Acta.* 50 (2005) 2603–2614.  
7 [57] R. Satija, D.L. Jacobson, M. Arif, S. a. Werner, In situ neutron imaging  
8 technique for evaluation of water management systems in operating PEM fuel  
9 cells, *J. Power Sources.* 129 (2004) 238–245.  
10 [58] H. Murakawa, K. Sugimoto, K. Miyata, H. Asano, N. Takenaka, Y. Saito,  
11 Visualization of Water Behavior in the In-plane and Throughplane Directions in  
12 a PEFC using a Neutron Image Intensifier, *Phys. Procedia.* 43 (2013) 277–  
13 281.  
14 [59] A.B. Geiger, A. Tsukada, E. Lehmann, P. Vontobel, A. Wokaun, G.G. Scherer,  
15 In Situ Investigation of Two-Phase Flow Patterns in Flow Fields of PEFC ' s  
16 Using Neutron Radiography, (2002) 92–98.  
17 [60] J.M. LaManna, S. Chakraborty, J.J. Gagliardo, M.M. Mench, Isolation of  
18 transport mechanisms in PEFCs using high resolution neutron imaging, *Int. J.*  
19 *Hydrogen Energy.* 39 (2014) 3387–3396.  
20 [61] H. Iwase, S. Koizumi, H. Iikura, M. Matsubayashi, D. Yamaguchi, Y. Maekawa,  
21 et al., A combined method of small-angle neutron scattering and neutron  
22 radiography to visualize water in an operating fuel cell over a wide length scale  
23 from nano to millimeter, *Nucl. Instruments Methods Phys. Res. Sect. A Accel.*  
24 *Spectrometers, Detect. Assoc. Equip.* 605 (2009) 95–98.  
25 [62] N. Pekula, K. Heller, P. a. Chuang, a. Turhan, M.M. Mench, J.S. Brenizer, et  
26 al., Study of water distribution and transport in a polymer electrolyte fuel cell  
27 using neutron imaging, *Nucl. Instruments Methods Phys. Res. Sect. A Accel.*  
28 *Spectrometers, Detect. Assoc. Equip.* 542 (2005) 134–141.  
29 [63] T.A. Trabold, J.P. Owejan, D.L. Jacobson, M. Arif, P.R. Huffman, In situ  
30 investigation of water transport in an operating PEM fuel cell using neutron  
31 radiography: Part 1 – Experimental method and serpentine flow field results,  
32 *Int. J. Heat Mass Transf.* 49 (2006) 4712–4720.  
33 [64] M.A. Hickner, N.P. Siegel, K.S. Chen, D.S. Hussey, D.L. Jacobson, M. Arif, In  
34 Situ High-Resolution Neutron Radiography of Cross-Sectional Liquid Water  
35 Profiles in Proton Exchange Membrane Fuel Cells, *J. Electrochem. Soc.* 155  
36 (2008) B427.  
37 [65] M.A. Hickner, K.S. Chen, N.P. Siegel, Elucidating Liquid Water Distribution and  
38 Removal in an Operating Proton Exchange Membrane Fuel Cell via Neutron  
39 Radiography, *J. Fuel Cell Sci. Technol.* 7 (2010) 011001.  
40 [66] C. Hartnig, I. Manke, N. Kardjilov, a. Hilger, M. Grünerbel, J. Kaczerowski, et  
41 al., Combined neutron radiography and locally resolved current density  
42 measurements of operating PEM fuel cells, *J. Power Sources.* 176 (2008)  
43 452–459.  
44 [67] A. Schmitz, M. Tranitz, S. Wagner, R. Hahn, C. Hebling, Planar self-breathing  
45 fuel cells, *J. Power Sources.* 118 (2003) 162–171.  
46 [68] R. Hahn, S. Wagner, A. Schmitz, H. Reichl, Development of a planar micro fuel  
47 cell with thin film and micro patterning technologies, *J. Power Sources.* 131  
48 (2004) 73–78.  
49 [69] S.U. Jeong, E.A. Cho, H.-J. Kim, T.-H. Lim, I.-H. Oh, S.H. Kim, A study on  
50 cathode structure and water transport in air-breathing PEM fuel cells, *J. Power*  
51 *Sources.* 159 (2006) 1089–1094.  
52  
53  
54  
55  
56  
57  
58  
59  
60  
61  
62  
63  
64  
65

- 1  
2  
3  
4 [70] S.U. Jeong, E.A. Cho, H.-J. Kim, T.-H. Lim, I.-H. Oh, S.H. Kim, Effects of  
5 cathode open area and relative humidity on the performance of air-breathing  
6 polymer electrolyte membrane fuel cells, *J. Power Sources*. 158 (2006) 348–  
7 353.  
8  
9 [71] N. Bussayajarn, H. Ming, K.K. Hoong, W.Y. Ming Stephen, C.S. Hwa, Planar air  
10 breathing PEMFC with self-humidifying MEA and open cathode geometry  
11 design for portable applications, *Int. J. Hydrogen Energy*. 34 (2009) 7761–  
12 7767.  
13 [72] T. Fabian, R. O’Hayre, S. Litster, F.B. Prinz, J.G. Santiago, Passive water  
14 management at the cathode of a planar air-breathing proton exchange  
15 membrane fuel cell, *J. Power Sources*. 195 (2010) 3201–3206.  
16 [73] D.T.S. Rosa, D.G. Pinto, V.S. Silva, R.A. Silva, C.M. Rangel, High performance  
17 PEMFC stack with open-cathode at ambient pressure and temperature  
18 conditions, *Int. J. Hydrogen Energy*. 32 (2007) 4350–4357.  
19 [74] J. Wu, S. Galli, I. Lagana, A. Pozio, G. Monteleone, X. Zi, et al., An air-cooled  
20 proton exchange membrane fuel cell with combined oxidant and coolant flow,  
21 *J. Power Sources*. 188 (2009) 199–204.  
22 [75] G. Jung, K. Lo, A. Su, F. Weng, C. Tu, T. Yang, et al., Experimental evaluation  
23 of an ambient forced-feed air-supply PEM fuel cell, *Int. J. Hydrogen Energy*. 33  
24 (2008) 2980–2985.  
25 [76] A.P. Sasmito, E. Birgersson, K.W. Lum, A.S. Mujumdar, Fan selection and  
26 stack design for open-cathode polymer electrolyte fuel cell stacks, *Renew.*  
27 *Energy*. 37 (2012) 325–332.  
28 [77] B. Kim, Y. Lee, A. Woo, Y. Kim, Effects of cathode channel size and operating  
29 conditions on the performance of air-blowing PEMFCs, *Appl. Energy*. 111  
30 (2013) 441–448.  
31 [78] H. Guo, M. Hai, F. Ye, C. Fang, Experimental study of temperature distribution  
32 on anodic surface of MEA inside a PEMFC with parallel channels flow bed, *Int.*  
33 *J. Hydrogen Energy*. 37 (2012) 13155–13160.  
34 [79] C. Wen, G. Huang, Application of a thermally conductive pyrolytic graphite  
35 sheet to thermal management of a PEM fuel cell, *J. Power Sources*. 178  
36 (2008) 132–140.  
37 [80] Q. Meyer, K. Ronaszegi, J.B. Robinson, M. Noorkami, O. Curnick, S. Ashton, et  
38 al., Combined Current and Temperature Mapping in an Air-Cooled, Open-  
39 Cathode Polymer Electrolyte Fuel Cell Under Steady-State and Dynamic  
40 Conditions., *J. Power Sources*, *in Press*. (2015).  
41 [81] E.H. Lehmann, P. Vontobel, L. Wiesel, Properties of the radiography facility  
42 neutral at SINQ and its potential for use as European reference facility,  
43 *Nondestruct. Test. Eval*. 16 (2001) 191–202.  
44 [82] P. Boillat, P. Oberholzer, a. Kaestner, R. Siegrist, E.H. Lehmann, G.G. Scherer,  
45 et al., Impact of Water on PEFC Performance Evaluated by Neutron Imaging  
46 Combined with Pulsed Helox Operation, *J. Electrochem. Soc*. 159 (2012)  
47 F210–F218.  
48 [83] P. Boillat, Advanced characterization of polymer electrolyte fuel cells using high  
49 resolution neutron imaging, ETH, 2009.  
50 [84] A. Iranzo, P. Boillat, Liquid water distribution patterns featuring back-diffusion  
51 transport in a PEM fuel cell with neutron imaging, *Int. J. Hydrogen Energy*. 39  
52 (2014) 17240–17245.  
53  
54  
55  
56  
57  
58  
59  
60  
61  
62  
63  
64  
65

- 1  
2  
3  
4 [85] D.J. Ludlow, C.M. Calebrese, S.H. Yu, C.S. Dannehy, D.L. Jacobson, D.S.  
5 Hussey, et al., PEM fuel cell membrane hydration measurement by neutron  
6 imaging, *J. Power Sources*. 162 (2006) 271–278.  
7 [86] J. Owejan, T. Trabold, D. Jacobson, M. Arif, S. Kandlikar, Effects of flow field  
8 and diffusion layer properties on water accumulation in a PEM fuel cell, *Int. J.*  
9 *Hydrogen Energy*. 32 (2007) 4489–4502.  
10 [87] P. Oberholzer, P. Boillat, Local Characterization of PEFCs by Differential Cells:  
11 Systematic Variations of Current and Asymmetric Relative Humidity, *J.*  
12 *Electrochem. Soc.* 161 (2013) F139–F152.  
13 [88] Q. Meyer, K. Ronaszegi, G. Pei-June, O. Curnick, S. Ashton, T. Reisch, et al.,  
14 Optimisation of air cooled, open-cathode fuel cells: Current of lowest  
15 resistance and electro-thermal performance mapping, *J. Power Sources*. 291  
16 (2015) 261–269.  
17 [89] R. O’Hayre, T. Fabian, S. Litster, F.B. Prinz, J.G. Santiago, Engineering model  
18 of a passive planar air breathing fuel cell cathode, *J. Power Sources*. 167  
19 (2007) 118–129.  
20 [90] Q. Meyer, A. Himeur, S. Ashton, O. Curnick, R. Clague, T. Reisch, et al.,  
21 System-Level Electro-thermal Optimisation of Air-Cooled Open-Cathode  
22 Polymer Electrolyte Fuel Cells: Air Blower Parasitic Load and Schemes for  
23 Dynamic Operation., *Int. J. Hydrog. Energy*. (*in Press*).  
24  
25  
26  
27  
28  
29  
30  
31  
32  
33  
34  
35  
36  
37  
38  
39  
40  
41  
42  
43

44 **List of Figures:**  
45  
46  
47

48 Figure 1. (a) Simplified Schematic and picture (b) of the fuel cell set-up for through-plane  
49 measurement in NEUTRA [81], facing the LiF/ZnS scintillator.  
50  
51  
52  
53

54 Figure 2. (a) Neutron imaging at open circuit potential, (b) neutron image at  $0.5 \text{ A cm}^{-2}$ ,  $5.6 \times$   
55  $10^{-3} \text{ m}^3 \text{ s}^{-1}$ ; (c) cross-section of the two-cell stack; (d) corresponding through-plane image.  
56  
57  
58  
59  
60  
61  
62  
63  
64  
65

1  
2  
3  
4  
5 Figure 3. Hydro-electro-thermal profile of the cell, displaying the “electro-thermal” and  
6 “hydro-thermal” maps. (a-f) correspond to representative zones of operation discussed in the  
7 text. The saw-tooth shape at high current density is an artefact of the extrapolation.  
8  
9

10  
11  
12 Figure 4. Localised hydro-electro-thermal maps at points (a) and (b) from Figure 3. The  
13 green arrow represents the air flow from inlet to exhaust, the red arrow the hydrogen flow  
14 from inlet to exhaust. (a, air flow rate of  $5.6 \times 10^{-3} \text{ m}^3 \text{ s}^{-1}$ ; b,  $4.7 \times 10^{-3} \text{ m}^3 \text{ s}^{-1}$ ).  
15  
16  
17  
18  
19

20  
21 Figure 5. Localised hydro-electro-thermal maps at points (c) and (d) from Figure 4. The  
22 green arrow represents the air flow from inlet to exhaust, the red arrow the hydrogen flow  
23 from inlet to exhaust. The dashed boxes in the hydro map are further discussed in Figure 6.  
24  
25  
26 (c, air flow rate of  $5.6 \times 10^{-3} \text{ m}^3 \text{ s}^{-1}$ ; d,  $3.9 \times 10^{-3} \text{ m}^3 \text{ s}^{-1}$ ).  
27  
28  
29

30  
31 Figure 6. Close up view of the areas of the hydro maps, in (c) and (d) highlighted in Figure 5,  
32 and average corresponding water thickness.  
33  
34  
35

36  
37 Figure 7. Localised hydro-electro-thermal maps at points (e) and (f) from Figure 3. The green  
38 arrow represents the air flow, the red arrow the hydrogen flow directions. The dashed ellipse  
39 on the hydro map of (f) is used as a guide for the eye. (e, air flow rate of  $4.7 \times 10^{-3} \text{ m}^3 \text{ s}^{-1}$ ; f,  
40  
41  
42  
43  
44  
45  
46  
47  
48  
49  
50  
51  
52  
53  
54  
55  
56  
57  
58  
59  
60  
61  
62  
63  
64  
65

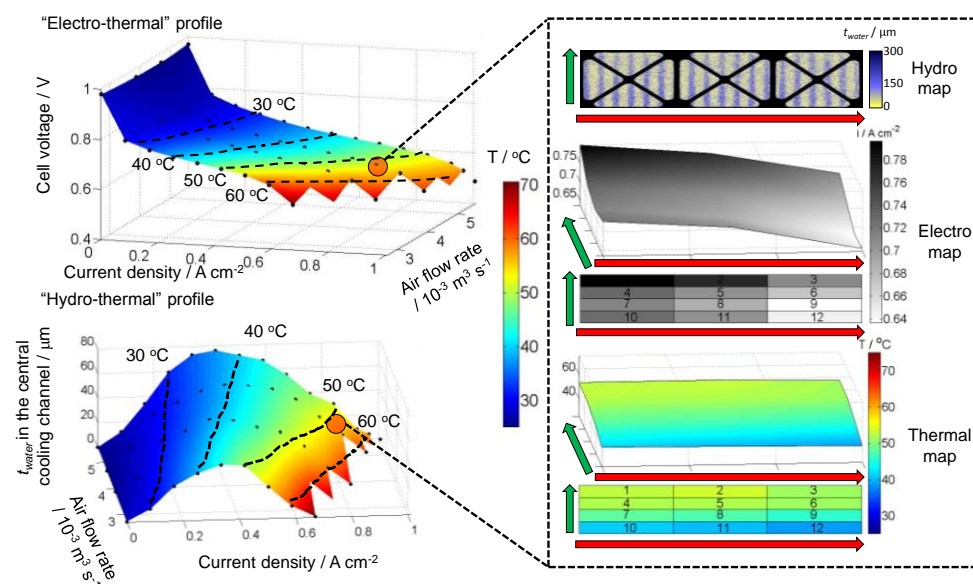
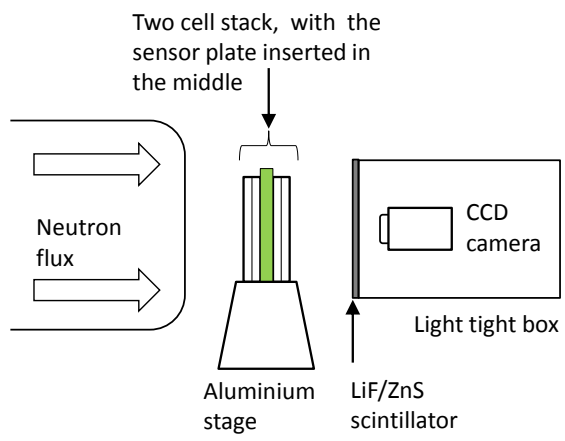
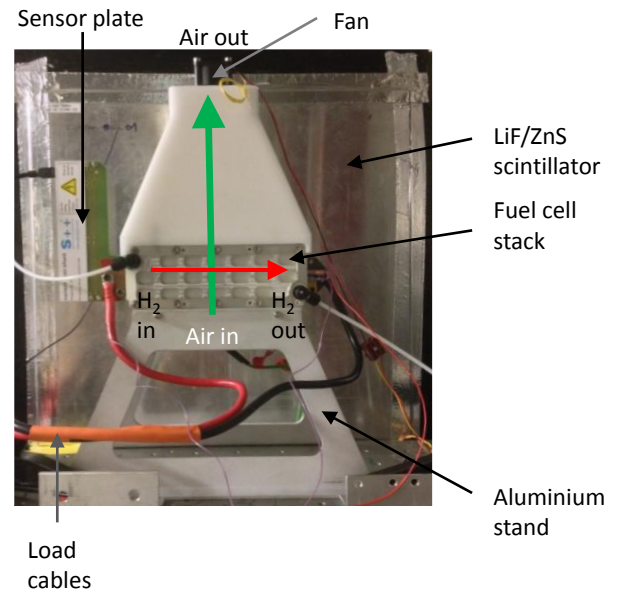


Figure 1



(a)



(b)

Figure 2

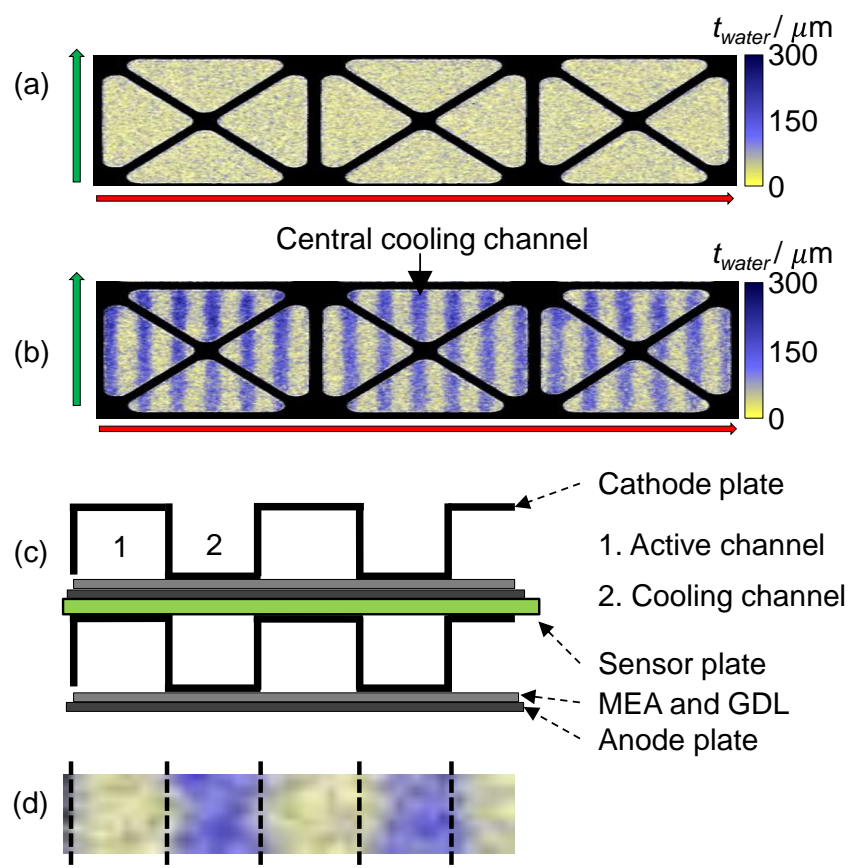
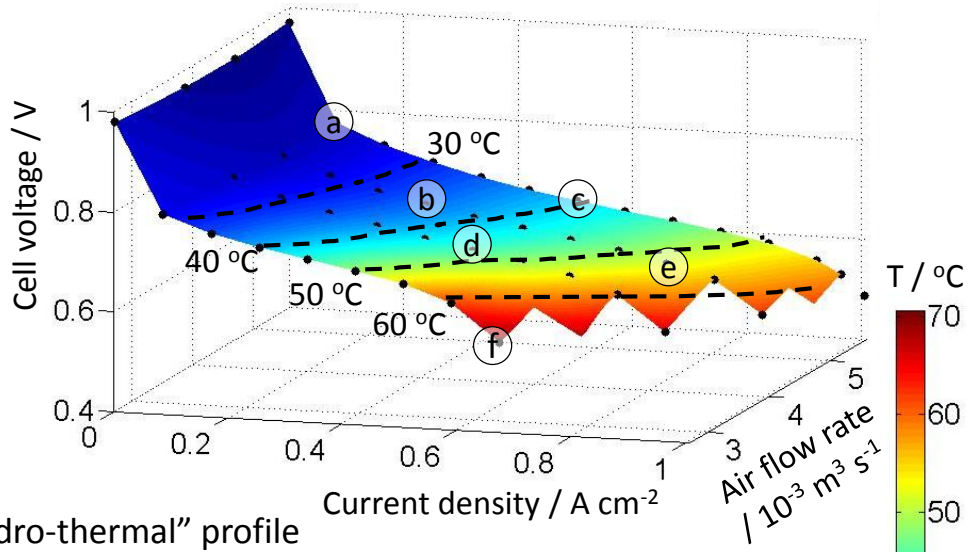


Figure 3

“Electro-thermal” profile



“Hydro-thermal” profile

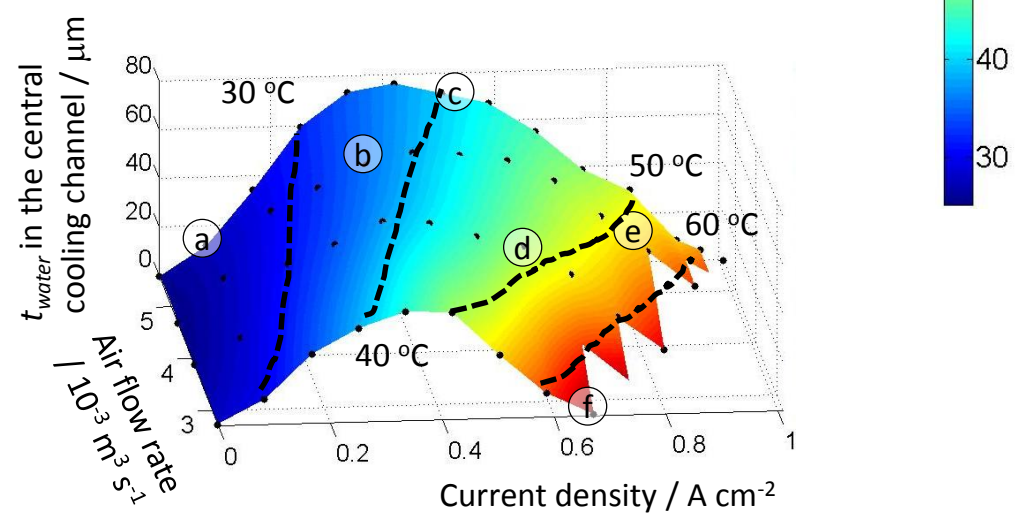


Figure 4

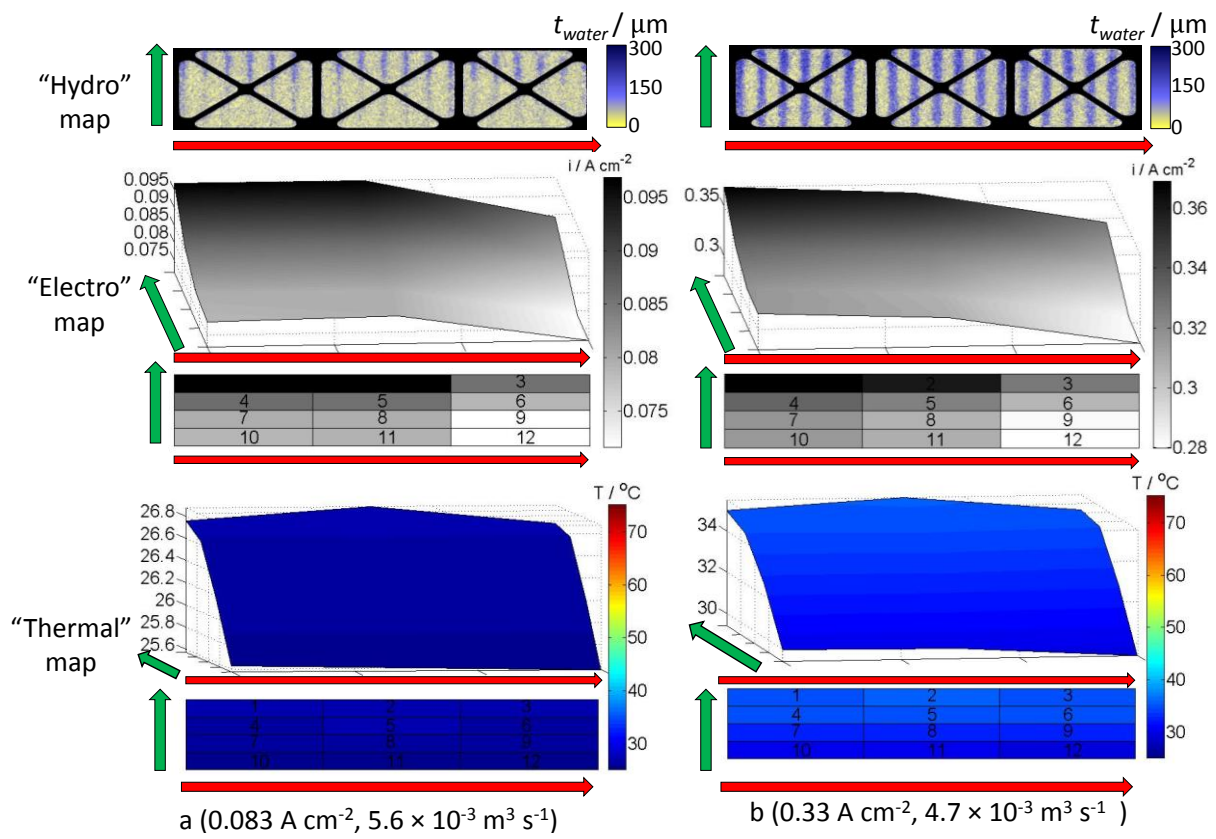


Figure 5

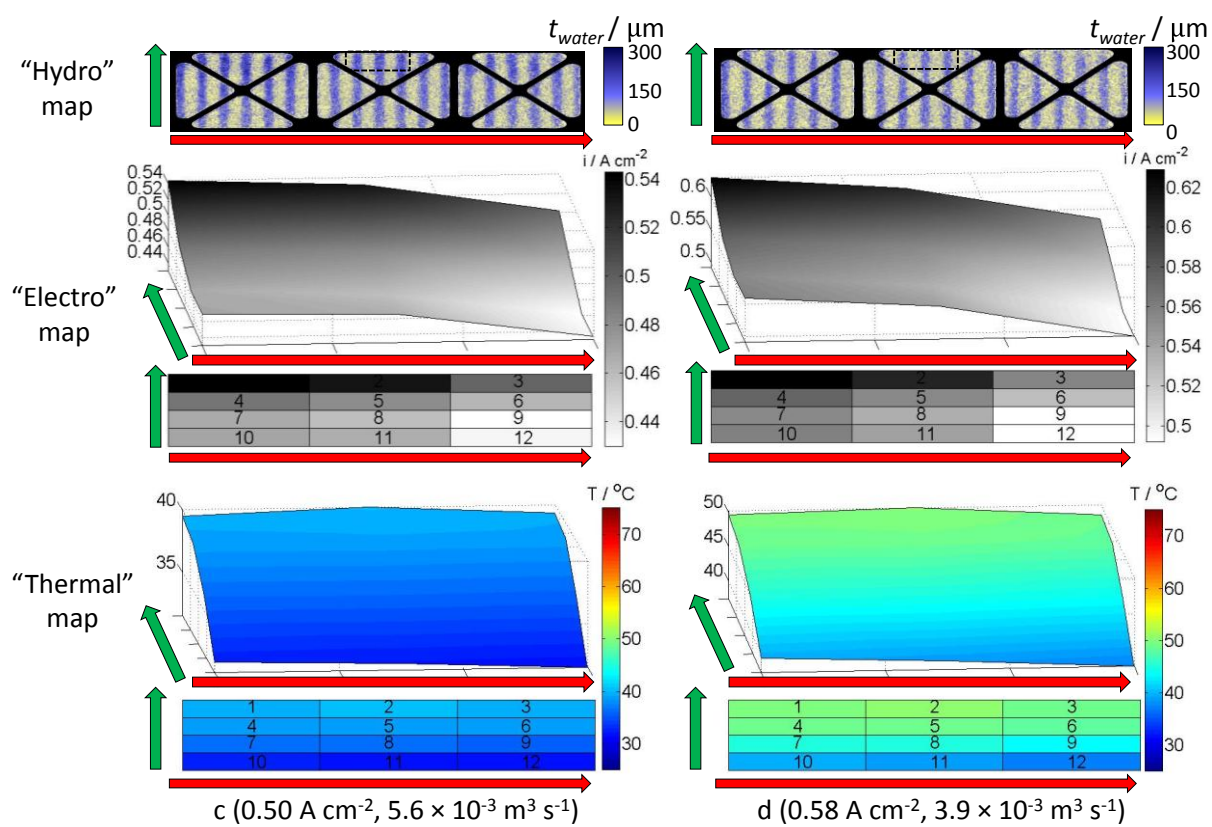


Figure 6

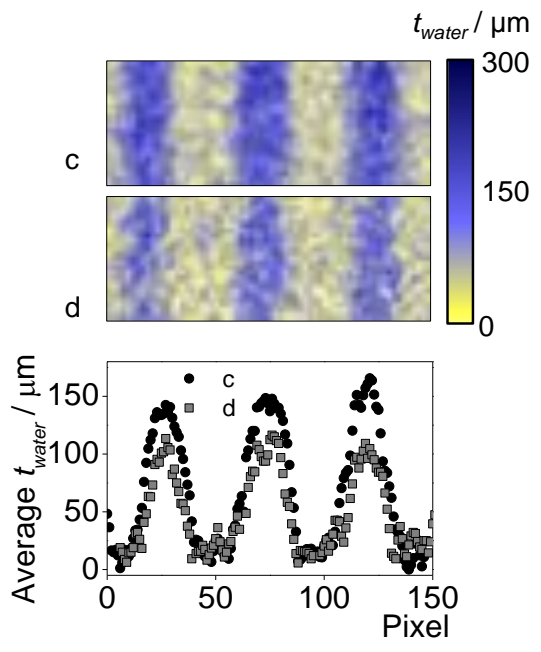


Figure 7

